

Effect of coherent and incoherent precipitates upon the stress and strain fields of 6xxx aluminium alloys: a numerical analysis

Muhammad Zain-ul-abdein · Daniel Nélías

Received: 27 November 2014 / Accepted: 23 February 2015 / Published online: 27 February 2015
© Springer Science+Business Media Dordrecht 2015

Abstract This paper investigates the stress and strain fields induced by the coherent/incoherent precipitates of type Mg_xSi_y in the 6xxx series aluminium alloys using numerical means. During welding of 6xxx series alloys, the heat-affected zone experiences high temperature heating and cooling cycles and hence results in the non-uniform stress and strain states both at macro- and micro-scales. In the present work, the macro-scale finite element (FE) simulations were carried out to calculate and compare the bulk material properties with those of experimental findings. Since the microstructure of 6xxx alloys comprises mostly of soft α -matrix and coherent/incoherent Mg_xSi_y precipitates, the properties of the individual constituents were used to perform micro-scale FE simulations. Temperature dependent theoretical yield strengths for the precipitates were also determined. The simulated micro-stress and strain fields showed strong dependency over the nature (coherent/incoherent), shape morphology (needle-like, random etc.) and distribution of precipitates. Additionally, unlike coherent precipitates, the plastic deformation of the matrix due

to incoherent impurities was found to be highly non-uniform and localized. FE analysis was also performed to characterize the effect of grain size upon the stress state of material.

Keywords Micro-scale simulation · 6xxx aluminium alloys · Coherent/incoherent precipitates · Grain size · Stress field · Strain field

1 Introduction

The 6xxx series aluminium alloys are used extensively in the aircraft structures due to their high strength and weldability (Heinz et al. 2000; Liu and Kulak 2000; Bardel et al. 2014). For instance, the fuselage panels in the new generation airplanes are being manufactured with AA6056 and AA6061 using laser beam and friction stir welding techniques. However, welding process exposes the aluminium sheets to temperatures as high as the melting temperature. Upon solidification, the weld bead and the adjacent heat affected zone (HAZ) possess complex microstructures, which, in turn, have strong influence upon the residual stress and strain states. Generally, a non-uniform state of stress is a major cause of failure or excessive deformation of the aircraft structure. Knowing the stress and strain fields at microscopic level is, therefore, of interest from the perspective of structure design and fabrication.

M. Zain-ul-abdein (✉)
Department of Mechanical Engineering, Faculty of
Engineering – North Jeddah Campus, King Abdulaziz
University, Jeddah, Saudi Arabia
e-mail: mzainulabdein@gmail.com

D. Nélías
INSA-Lyon, LaMCoS UMR5259, Université de Lyon,
CNRS, Lyon, France

Recently, several studies have been devoted to investigating the microstructural changes in 6xxx (Al–Mg–Si based) alloys and their effects upon the mechanical and physical properties (Sharma 2000; Chakrabarti and Laughlin 2004; Asserin-Lebert et al. 2005; Cicala et al. 2005; Cavaliere et al. 2006; Cabibbo et al. 2007; Gallais et al. 2008). In Al–Mg–Si alloys, the alloying additions dissolve into an Al-rich single phase solid solution (α) at high temperature, while at room temperature the α -phase is in a super-saturated state and hence, in order to achieve equilibrium, it must precipitate out second phase Mg_xSi_y grains in the form of Guinier–Preston (GP) zone, β'' , β' and β particles. GP zones are usually the first precipitates to appear in naturally aged (T4 temper) and precipitation hardened (T6 temper) alloys. Their formation is followed by the precipitation of coherent β'' and semi-coherent β' grains. It has been reported in literature (Porter and Easterling 1992; Edwards et al. 1998; Miao and Laughlin 1999; Matsuda et al. 2003) that these precipitates are responsible for the strengthening of 6xxx series alloys. The α -phase reaches equilibrium only upon the formation of incoherent β (Mg_2Si) precipitates. Here, the equilibrium α -phase is the softest phase and said to have an ‘O’ temper state. The temperature dependent elastic–plastic properties of the 6xxx series alloys in T4, T6 and O temper states have already been published by some researchers (Schwartzberg et al. 1970; Ledbetter 1982; ASM International 2002; Zain-ul-abdein et al. 2010a, b; Nélias et al. 2014).

Numerical means are generally required where the use of experimental methods is either practically impossible or economically infeasible. The finite element (FE) modeling of the welding induced distortions and stresses in 6xxx series alloys has been the subject of many recent publications (Darcourt et al. 2004; Josserand et al. 2007; Zain-ul-abdein et al. 2010a, b; Riahi and Nazari 2011; Zhang et al. 2014). Most of these works predict stress and strain states at macroscopic level. This means that the simulated results assume homogeneity of the bulk material. While in reality, the material with α -matrix and Mg_xSi_y precipitates is microscopically heterogeneous. It is rare to find any literature that divulges the effect of Mg_xSi_y precipitates upon the stress and strain fields of 6xxx series alloys. Radaj (1992), however, categorized these macro- and micro-stresses as first order (σ^I), second order (σ^{II}) and third order (σ^{III}) stresses.

Here, σ^I refers to the macro-stress averaged over a volume of several material grains, σ^{II} represents micro-stress between the grains of matrix and precipitates, while σ^{III} corresponds to the inter-atomic stress due to impurity atom, vacancy, Frenkel defect etc.

In the first part of the present work, a 2D macro-scale simulation was performed for a tensile test specimen and the results for true stress–strain curves were compared with the experimental ones. In the second part, the emphasis is placed upon the computation of the stress and strain distribution at microscopic level in 2D by the coherent and incoherent precipitates. Note that no distinction was made between the coherent and semi-coherent particles during simulation. This is because, the coherent and semi-coherent precipitates differ from each other on account of coherency strains only; yet both of them increase the overall strength of the material. Simulating coherency strains is beyond the scope of the present work. Incoherent precipitates, on the other hand, result in the overall reduced strength of the material. In addition, the grain size effects upon the deformation behavior have also been investigated.

2 Experimental data

Most of the data required for the numerical analysis was obtained from the published works. Zain-ul-abdein et al. (2010a, b) reported experimentally determined true stress–strain curves for AA6056-T4 at temperatures ranging from 16 to 450 °C with different strain rates. They have carried out tensile tests using specimens made out of thin sheets of thickness 2.5 mm. The specimens were heated at a temperature rate of 25 °C/s up to the test temperature by electrical Joule heating.

In their work, Maisonnette et al. (2011) and Nélias et al. (2014) reported the true stress–strain curves for AA6061 in O tempered state corresponding to the soft α -phase. They proposed a model for calculating the yield strength of O-tempered specimens from 20 to 550 °C. They have also shown that the hardening behavior of the soft phase remains perfectly plastic over a wide range of temperature. Moreover, they have performed high resolution transmission electron microscopy to highlight the shape morphology of precipitates. Their findings showed that the precipitate

volume fraction reached up to 1.6 %. The reported material properties of the soft α -phase are used in this work for micro-scale numerical simulations.

Note that the published data provides the thermo-elasto-plastic properties of the bulk homogeneous material in T4 (naturally aged) state as well as O-tempered state for the soft α -matrix. However, the material properties for the second phase Mg_xSi_y precipitates are not available and hence, they must be computed before the numerical simulation of micro-stresses of the heterogeneous medium.

3 Numerical analysis

A commercial FE code Abaqus was used to perform 2D macro-scale and micro-scale simulations, henceforth called macro-simulation and micro-simulation, respectively. As mentioned earlier, the macro-simulation assumes homogeneous material properties, whereas the micro-simulation considers heterogeneous structure with different material properties of the α -matrix and Mg_xSi_y precipitates.

3.1 Macro-simulation

The geometry and the mesh of the tensile test specimen are shown in Fig. 1. Since the original specimens were obtained from a sheet of thickness 2.5 mm (Zain-ul-abdein et al. 2010a, b), the plane stress conditions were assumed for the analysis. In addition, the specimen is axially symmetric, and hence a symmetric model was realized in order to reduce the total number of degrees of freedom. The entire model consisted of 7935 nodes and 7602 linear elements, where mostly 4-nodes quadrilateral elements (DC2D4E, CPS4R) were used while some 3-nodes triangular elements (DC2D3E, CPS3) were included to complete the mesh.

A coupled thermal-electrical analysis was performed first to compute the nodal temperatures, such that each test temperature was reached at a heating rate of 25 °C/s. Note that the test temperatures for tensile tests were 16, 100, 200, 300, 350, 400 and 450 °C. Obviously, 16 °C was merely the room temperature and hence did not require heating; rather it was defined as an initial temperature. The nodal temperature values, so calculated, were used as a predefined field

for mechanical analysis in order to obtain the stress versus strain response of the model. The specimen was deformed axially at a displacement rate of 3.3×10^{-3} mm/s. Since the deformation rate was significantly slow, the mechanical dissipation can be ignored. The simulated nodal temperature history at the mid-point of the 25 mm gauge length and the applied mechanical boundary condition as a function of time are also shown in Fig. 1.

3.1.1 Thermal-electrical model

Ohm’s law describes the flow of electric current as follows:

$$\vec{J} = \sigma^E \vec{E} = -\sigma^E \overrightarrow{\text{grad}}\varphi \tag{1}$$

where, \vec{J} is electrical current density in $A\ m^{-2}$, σ^E is the electrical conductivity in $\Omega^{-1}\ m^{-1}$, \vec{E} is the electric field intensity in $V\ m^{-1}$, φ is the electrical potential in V.

\vec{J} can be calculated by imposing the following boundary conditions:

$$\begin{aligned} \sigma^E \overrightarrow{\text{grad}}\varphi \cdot \vec{n} &= j(\varphi) \\ \varphi &= \varphi_o \end{aligned} \tag{2}$$

where, $j(\varphi)$ is the applied current density and φ_o is the prescribed electrical potential.

In order to calculate the temperature (T) distribution in space (x,y) and time (t), the solution of the following heat equation is required.

$$\text{div}\left(\lambda^t(T)\overrightarrow{\text{grad}}T\right) + P_{ec} = \rho(T)C_p(T)\frac{\partial T}{\partial t} \tag{3}$$

where, $\lambda^t(T)$ is the thermal conductivity in $W\ m^{-1}\ K^{-1}$, $\rho(T)$ is the density in $kg\ m^{-3}$, $C_p(T)$ is the specific heat in $J\ kg^{-1}\ K^{-1}$, all as a function of temperature. The term P_{ec} , which is the internal heat generation rate or the rate of electrical energy in $W\ m^{-3}$, can be stated as:

$$P_{ec} = \vec{J} \cdot \vec{E} = \overrightarrow{\text{grad}}\varphi \cdot \left(\sigma^E \overrightarrow{\text{grad}}\varphi\right) \tag{4}$$

Hence, the Eq. (3) takes the following form:

$$\begin{aligned} \text{div}\left(\lambda^t(T)\overrightarrow{\text{grad}}T\right) + \overrightarrow{\text{grad}}\varphi \cdot \left(\sigma^E \overrightarrow{\text{grad}}\varphi\right) \\ = \rho(T)C_p(T)\frac{\partial T}{\partial t} \end{aligned} \tag{5}$$

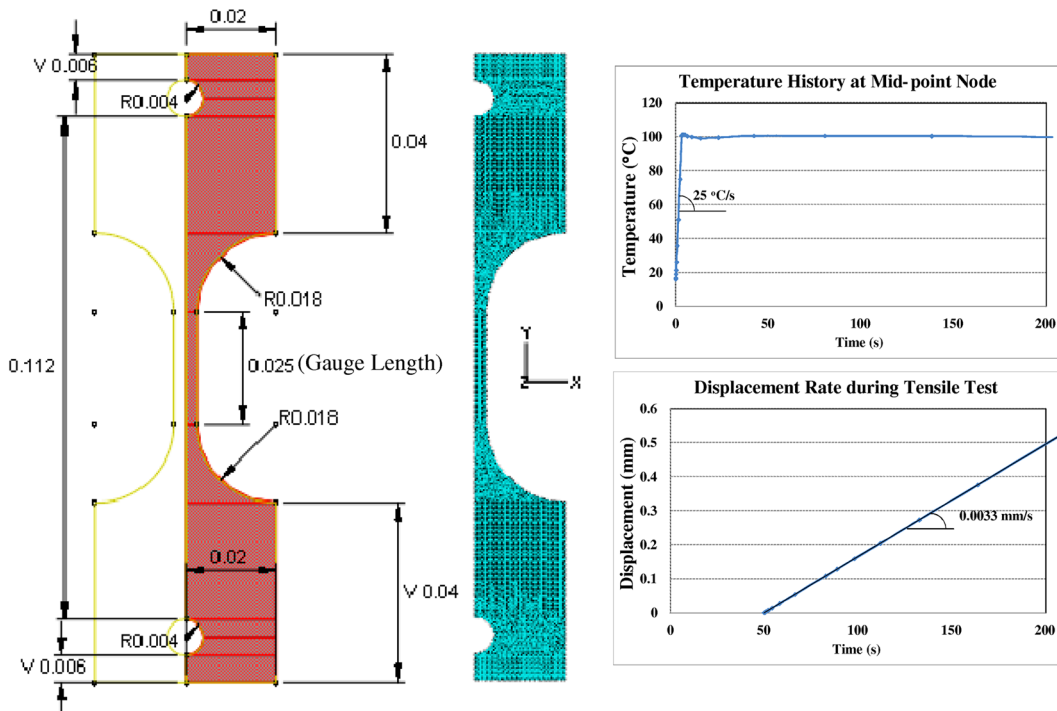


Fig. 1 Tensile test specimen geometry (dimensions in m), mesh, temperature history within gauge length and prescribed displacements at both ends

3.1.2 Mechanical model

Since the material was assumed to follow elasto-plastic behavior with isotropic hardening, the total strain tensor (ϵ^{total}) may be decomposed into thermal ($\epsilon^{thermal}$), elastic ($\epsilon^{elastic}$) and plastic ($\epsilon^{plastic}$) strains as follows:

$$\begin{aligned} \epsilon^{total} &= \epsilon^{thermal} + \epsilon^{elastic} + \epsilon^{plastic} \\ &= \alpha(T)(T - T_0)\mathbf{I} + \mathbf{C}^{-1}(T):\boldsymbol{\sigma} + \epsilon^{plastic} \end{aligned} \quad (6)$$

where, $\boldsymbol{\sigma}$ is the stress tensor, $\alpha(T)$ is the thermal expansion coefficient in K^{-1} , $\mathbf{C}^{-1}(T)$ is the inverse of 4th order stiffness tensor, $\mathbf{C}(T)$, and is defined in terms of Young's modulus, $E(T)$, and Poisson's ratio, $\nu(T)$, for an isotropic material. Note that all the properties are defined as a function of temperature.

For the plasticity criterion, yield function (f) to limit the elastic domain may be stated as follows:

$$f(\boldsymbol{\sigma}, T, R) < 0 \quad (7)$$

where, T is the temperature and R represents isotropic hardening parameter. The yield strength (σ_y) is defined

as $\sigma_y = \sigma_y(\epsilon^{plastic}, T)$, while the plastic flow of the material may be written in terms of plastic strain rate as:

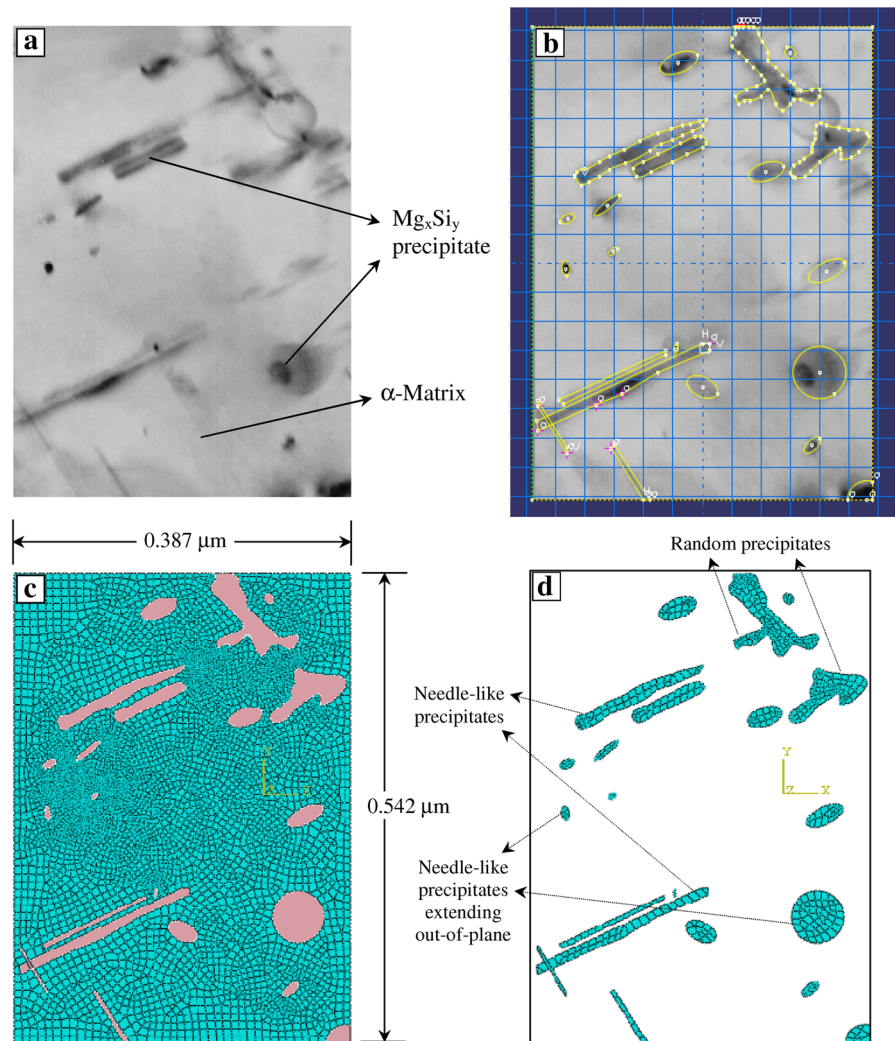
$$\begin{aligned} \dot{\epsilon}^{plastic} &= \dot{\lambda} \frac{dg}{d\boldsymbol{\sigma}} = \dot{\lambda} \frac{3}{2} \cdot \frac{\boldsymbol{\sigma}^D}{\sigma^{VM}} \quad \text{with} \\ \sigma^{VM} &= \sqrt{\frac{3}{2} \boldsymbol{\sigma}^D : \boldsymbol{\sigma}^D} \end{aligned} \quad (8)$$

Here, $g(\boldsymbol{\sigma}, T, R)$ is the flow potential, $\dot{\lambda}$ is the plastic flow rate whose value is determined by the requirement to satisfy the consistency condition $f = 0$, σ^{VM} is the von Mises effective stress and $\boldsymbol{\sigma}^D$ is the deviatoric stress tensor.

3.2 Micro-simulation

The microstructure under consideration (see Fig. 2a) is adopted from Maissonette et al. (2011), where the light colored background shows the α -matrix while Mg_xSi_y precipitates can be seen as dark colored needles. Note that the small circular precipitates are most likely the precipitate needles extending out-of-the-plane. The

Fig. 2 **a** Microstructure [from Maissonnette et al. (2011)], **b** geometry, **c** matrix mesh and **d** precipitate mesh



geometry of the microstructure over an area of $0.542 \mu\text{m} \times 0.387 \mu\text{m}$ is shown in Figs. 2b, whereas Fig. 2c, d illustrate the mesh of the α -matrix and the Mg_xSi_y precipitate, respectively. The mesh is composed of 6116 nodes and 6149 plane stress thermally coupled linear elements, which include 5864×4 -node quadrilateral elements with reduced integration (type: CPS4RT) and 285×3 -node triangular elements (type: CPS3T).

Given the predefined temperatures of 16, 100, 200, 300, 350, 400 and 450 °C, the left edge of the micro-mesh was constrained while the displacement rate of $3.3 \times 10^{-3} \text{ mm/s}$ was prescribed on the right edge along the $-x$ axis. It is to be mentioned that the elastic material properties of both the matrix and precipitates were assumed to be identical. Nevertheless, their yield

strength and hardening behavior were considered different from each other. For the soft α -matrix, the yield strength values with perfectly plastic hardening behavior were adopted from Nélias et al. (2014). For the precipitates, however, the yield strength values as a function of plastic strain and temperature have been calculated using theoretical models.

3.2.1 Theoretical yield strength of precipitates

According to Kocks et al. (1975) and Deschamps and Brechet (1999), the yield strength of an alloy depends upon (1) the friction stress (σ_o), (2) the matrix, or solid solution, contribution ($\Delta\sigma_m$) and (3) the precipitate contribution ($\Delta\sigma_p$). It follows:

$$\sigma_y = \sigma_o + \Delta\sigma_m + \Delta\sigma_p \tag{9}$$

where, σ_o for pure aluminium was found to be 10 MPa (Deschamps and Brechet 1999; Simar et al. 2012). The matrix and precipitate contribution factors are affected by the alloy composition and dislocation movement.

In order to define the relation among σ_y , σ_m , and σ_p , Nélías et al. (2014) proposed an equation of the form ‘Weiner model’ (Weiner 1912). Hence, at a given temperature:

$$M = \begin{cases} (1/e^2)\left(1 - \left(\sqrt{1 - e^2}/e\right) \arcsin e\right), & \text{if } c < a \text{ (oblate)} \\ (1 - e^2/2e^3)(\ln((1 + e)/(1 - e)) - 2e), & \text{if } c > a \text{ (prolate)} \end{cases}$$

$$M_{\perp} = (1 - M)/2, e = \sqrt{1 - \xi^2}, \xi = \begin{cases} c/a, & \text{if } c < a \text{ (oblate)} \\ a/c, & \text{if } c > a \text{ (prolate)} \end{cases}$$

$$\sigma_y = (1 - \phi_p)\sigma_m + \phi_p\sigma_p \tag{10}$$

where, σ_m is the yield strength of α -matrix (i.e. O-tempered soft phase), σ_p is the precipitate yield strength (i.e. Mg_xSi_y hard phase) and ϕ_p is the phase fraction of the precipitate. Weiner model, however, intrinsically assumes that only the volume fractions of each phase are known. A better approximation is in the form of Hashin and Shtrikman (1962) bounds, since they, in addition to the known phase fractions, also assume that the composite structure is macroscopically isotropic. The upper and lower bounds are:

$$\sigma_y \geq \sigma_m \left[1 + \frac{3\phi_p(\sigma_p - \sigma_m)}{3\sigma_m + (1 - \phi_p)(\sigma_p - \sigma_m)} \right] \text{ (lower bound)}$$

$$\sigma_y \leq \sigma_p \left[1 - \frac{3(1 - \phi_p)(\sigma_p - \sigma_m)}{3\sigma_p - \phi_p(\sigma_p - \sigma_m)} \right] \text{ (upper bound)}$$

$$\tag{11}$$

Nevertheless, Mori and Tanaka (1973) model based on effective field method is the most conservative one, where an inhomogeneity is treated as an isolated particle immersed into a homogeneous medium, i.e. the matrix. It is, therefore, suitable for the dilute concentration ($\phi_p < 10\%$) of inhomogeneity, which in the present case is $\phi_p = 1.6\%$. Additionally, it

introduces the depolarization factors (M_{\perp} , M), which also take into account the shape morphology of the impurities. The model states:

$$\sigma_y = \sigma_m + \frac{\phi_p(\sigma_p - \sigma_m)\beta}{(1 - \phi_p) + \phi_p\beta} \tag{12}$$

$$\text{where, } \beta = \frac{1}{3} \left(\frac{2\sigma_m}{\sigma_m + (\sigma_p - \sigma_m)M_{\perp}} + \frac{\sigma_m}{\sigma_m + (\sigma_p - \sigma_m)M} \right)$$

and

Here, c/a represents the ratio of the longitudinal axis to the transverse axis of the precipitate. For a needle like precipitate, the depolarization factors converge to $M_{\perp} = 1/2$ and $M = 0$.

Figure 3 summarizes the Mg_xSi_y precipitate yield strength (σ_p) as a function of temperature at $\epsilon^{plastic} = 0$ according to Eqs. 10, 11 and 12. It was observed that at T = 16 °C, the Weiner’s bound yielded a value of $\sigma_p = 9.64$ GPa; while Mori–Tanaka model gave $\sigma_p = 28.14$ GPa, which is three times as high as the

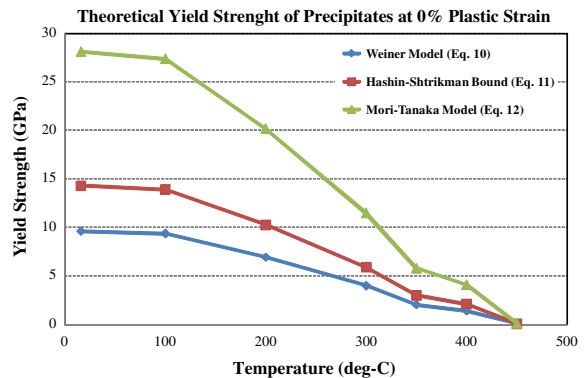


Fig. 3 Theoretical yield strength of Mg_xSi_y precipitates (σ_p) as a function of temperature at 0 % plastic strain

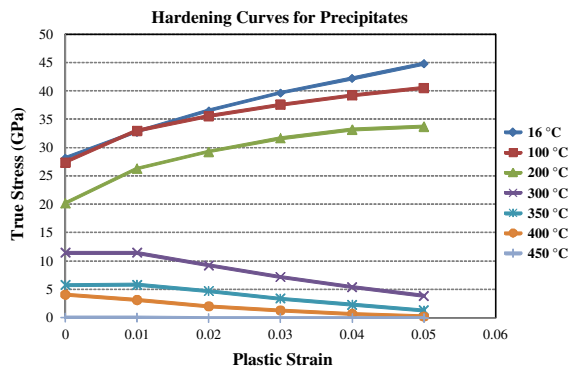


Fig. 4 Hardening curves for Mg_xSi_y precipitates as a function of temperature and plastic strain

former. For the reasons mentioned above, Mori–Tanaka equation was further used to obtain hardening curves as a function of plastic strain values (see Fig. 4).

3.2.2 Coherent and incoherent precipitates

Since the coherent/semi-coherent precipitates impart increased strength to 6xxx series alloys, it is of interest to observe their deformation at microscopic level. On the other hand, the incoherent precipitates result in the degradation of material properties, which implies that they offer little or no resistance to the deformation of parent matrix. In this work, the precipitates shown in Fig. 2d were modeled in two different ways: (1) deformable elements to assume coherency and (2) inactive elements to represent incoherency. It is to be mentioned that during welding, the heat-affected zone comprises almost all types of precipitates depending upon the acquired peak temperature (Gallais et al. 2008).

3.2.3 Grain size

The Hall–Petch model (Hall 1951; Petch 1953) is the most well-known relation to determine the effect of grain size (d) upon the yield strength (σ_y) of the material. It states:

$$\sigma_y(e^{plastic}, d) = \sigma_0 + K_{HP}(e^{plastic}) \cdot d^{-1/2} \quad (13)$$

where, K_{HP} is the strain dependent Hall–Petch material parameter in $MPa \mu m^{1/2}$. Clearly, the yield strength is a function of plastic strain and grain size.

Berbenni et al. (2007) pointed out that the Hall–Petch relation is widely accepted for heterogeneous material when the mean grain size is greater than ~ 100 nm, while the change in yield strength is increasingly susceptible to the distribution of grains from micro- to nano-scale. One of the consequences of welding is the coarsening of grain size in the HAZ. Figure 5a indicates a typical microstructure of laser welded AA6xxx plate, where the grain size reaches up to $200 \mu m$. Although the elongated shape of the grains is mainly due to the prior rolling of the plate, yet their effect upon the yield strength is unavoidable. In the present work, it has been assumed that the grain size in the HAZ varies from 10 to $200 \mu m$. Using Eq. 13 along with the material properties of α -matrix, the parameter K_{HP} was calculated and shown in Fig. 5b. Note that the K_{HP} yields insignificantly smaller values for the grain size of $0.1 \mu m$.

4 Results and discussion

4.1 Stress–strain curves

The results of the macro-simulation are shown in Figs. 6 and 7. Figure 6 presents the nodal temperature as well as von Mises stress contours in the tensile test specimen when the temperature of $100 \text{ }^\circ\text{C}$ was reached. It is to be noted that the desired temperature and maximum stress are present in the middle of the specimen gauge length, where the cross-section area is minimum. Although several simulations were run for different test temperatures (16, 200, 300, 350, 400 and $450 \text{ }^\circ\text{C}$), Fig. 6 is a representative of the stress and temperature distributions for all of them. Nevertheless, the contour values were different for all the simulations. Figure 7 reports the simulated stress–strain curves obtained for all the test temperatures. In addition, a comparison is developed with reference to the experimental results, provided elsewhere in Zain-ul-abdein et al. (2010a, b). A good agreement was found between the experimental and simulated results. Note that the stress–strain curves from 16 to $200 \text{ }^\circ\text{C}$ show decreasing strength values at a given plastic strain. This is because the increase in temperature results in an increased mobility of dislocations, thereby reducing the overall strength of the material. However, the hardening slopes remain the same over the temperature range (16– $200 \text{ }^\circ\text{C}$). This observation

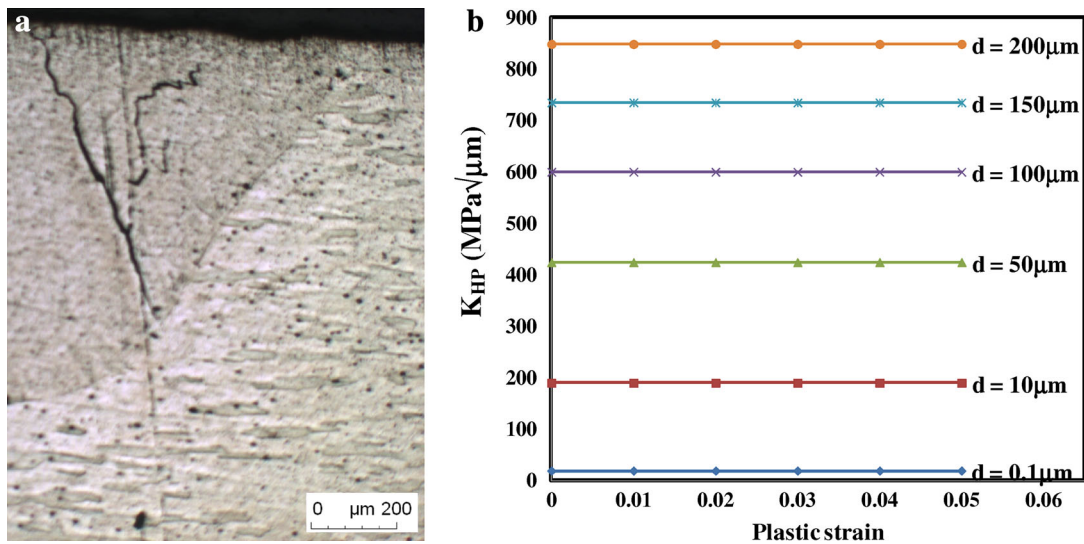
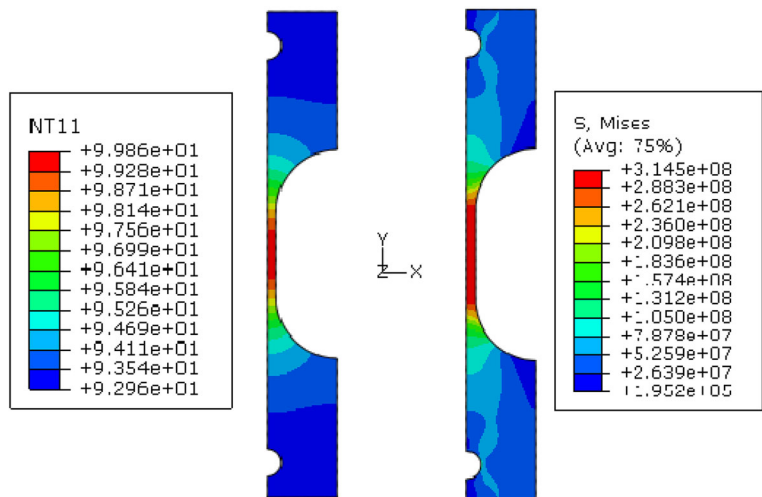


Fig. 5 **a** Microstructure of a typical AA6xxx laser welded specimen; **b** Hall–Petch parameter (K_{HP}) as a function of plastic strain and grain size (d)

Fig. 6 Nodal temperature in $^{\circ}\text{C}$ (*left*) and von Mises stress contours in MPa (*right*) for the tensile test specimen



indicates that hard coherent precipitates survive at least up to 200 $^{\circ}\text{C}$ and they even impart significant strength to the alloy by interlocking the dislocations. There is, however, a sudden drop in the overall strength as well as the hardening slopes at temperatures ranging from 300 to 450 $^{\circ}\text{C}$. At such high temperatures, the predominant phenomena are the dislocation glide and climb, while the impurities offer little or no resistance due to their decreased strength or dissolution in parent matrix. It may also be observed from Figs. 3 and 4 that the theoretical yield strengths

and hardening slopes drop off to negligibly small values as the temperature increases.

4.2 Coherent precipitates: stress fields

The effect of coherent precipitates (β'' , β') over the micro-stress fields is shown in Fig. 8. Here, the von Mises effective stress (σ^{VM}) within the matrix and coherent precipitates at temperatures 100 and 450 $^{\circ}\text{C}$ are revealed. Note that the stress level in α -matrix at 100 $^{\circ}\text{C}$ ranges from 28.1 to 67 MPa (Fig. 8a), where

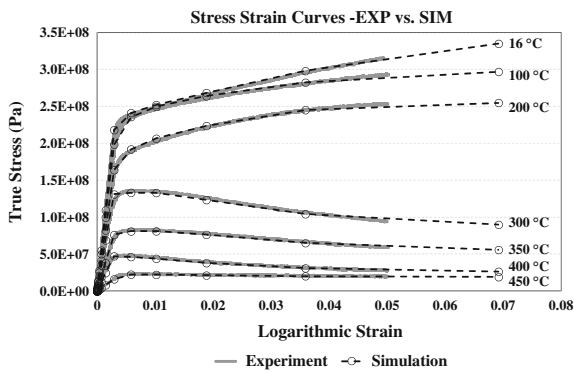
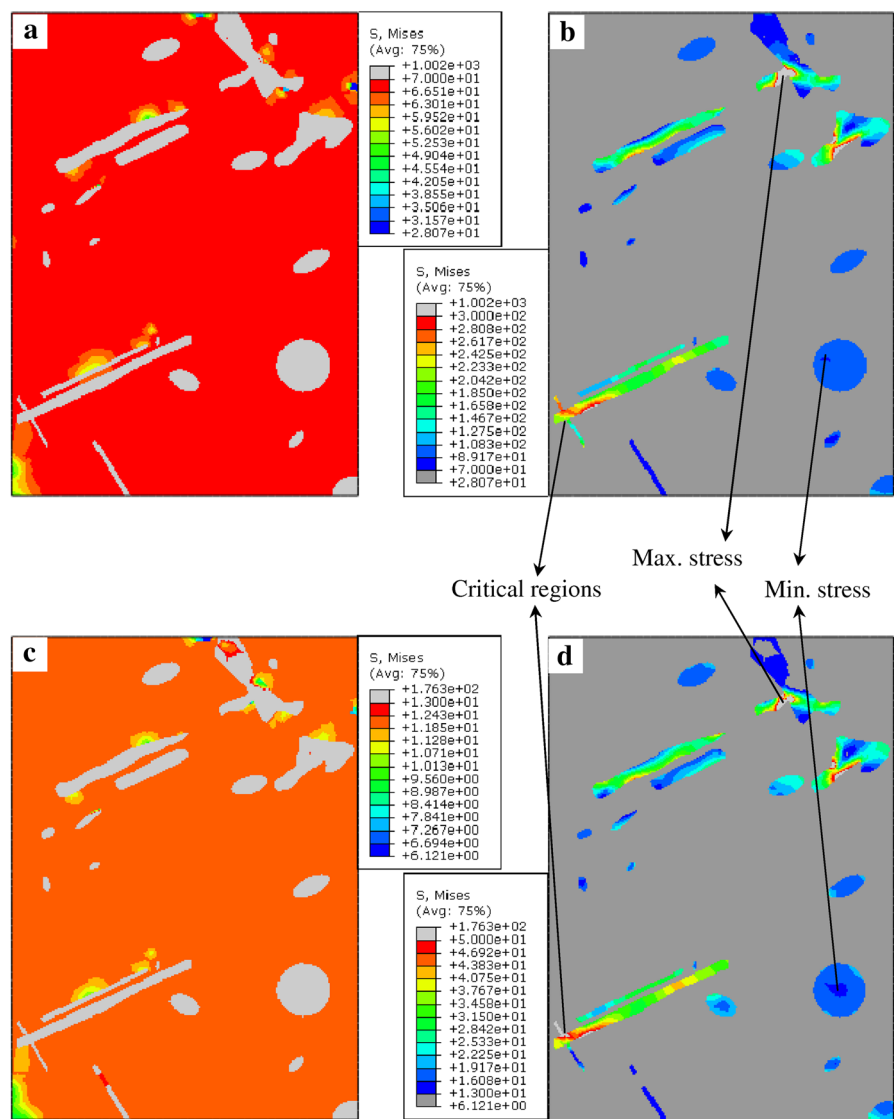


Fig. 7 Comparison of stress–strain curves for AA6056—Experiment [from Zain-ul-abdein et al. (2010a, b)] versus FE simulation

almost 95 % of the region shows stress values between 65 and 67 MPa. Only a few elements in the vicinity of the hard needle-like and random precipitates show a relatively lower stress level. Also note that the σ^{VM} in coherent precipitates at 100 °C lies between 42.6 and 1002 MPa (Fig. 8b). It may be observed that the maximum stress of 1002 MPa is present only in random precipitates, the needle-like precipitates show peak stress level of 328 MPa, while the needle-like precipitates protruding out-of-plane bear a minimum stress value of 97.5 MPa. Here, an interesting observation is that the difference in minimum and maximum stress is more than ten times; moreover, it

Fig. 8 Von Mises stress (MPa) contours in **a** matrix at 100 °C, **b** coherent precipitate at 100 °C, **c** matrix at 450 °C and **d** coherent precipitate at 450 °C



is solely dependent upon the shape and size of the coherent precipitates. It is to be mentioned that random precipitates are in reality several coalesced needle-like precipitates, and that the needle-like precipitates extending out-of-plane behave in a manner similar to the in-plane circular impurities.

While the displacement was prescribed normal to the right edge of microstructure, the stress is distributed along the longitudinal axis of the needle-like precipitates. In case of random impurities, the maximum stress appears where the precipitate width is smallest. Clearly, this is the region where the material failure is more likely to initiate provided no other discontinuities like blowholes, notches etc. are present. The circular/near-circular heterogeneities offer uniformly distributed minimum stress in the radial direction. This implies that the material's resistance to deformation may be improved by introducing circular precipitates and avoiding random precipitates within the matrix. There are, however, some critical regions where, instead of complete coalescence, two or more needle-like precipitates interact to form 'partial coalescence'. Excluding random impurities, the stress at or near the point of interaction remains the highest (around 328 MPa in the present case). Figure 8c, d illustrate von Mises stress in the matrix and precipitate at 450 °C; note the similarity between the contours with those of Fig. 8a, b. Here, the only difference is in the stress values, which range from 6.12 to 12 MPa in matrix and from 8.43 to 176.3 MPa in precipitates.

4.3 Incoherent precipitates: stress fields

It is a well-established fact that the incoherent precipitates (β) in Al alloys result in the decrease of strength and hardness (Porter and Easterling 1992; Silcock et al. 1954). This is because the dislocations need an extra stress to pass through coherent precipitates. Due to the coherency loss, however, the dislocations bend around the precipitates and the matrix deforms with relative ease. Figure 9 illustrates the von Mises stress fields in the parent matrix with incoherent precipitates at temperatures 16, 200, 350 and 450 °C. Compared to the stress distribution in the matrix with coherent precipitates (Fig. 8), the stress field is highly non-uniform in the present case. This was an expected outcome since the coherent precipitates offer a continuity of the medium; while the

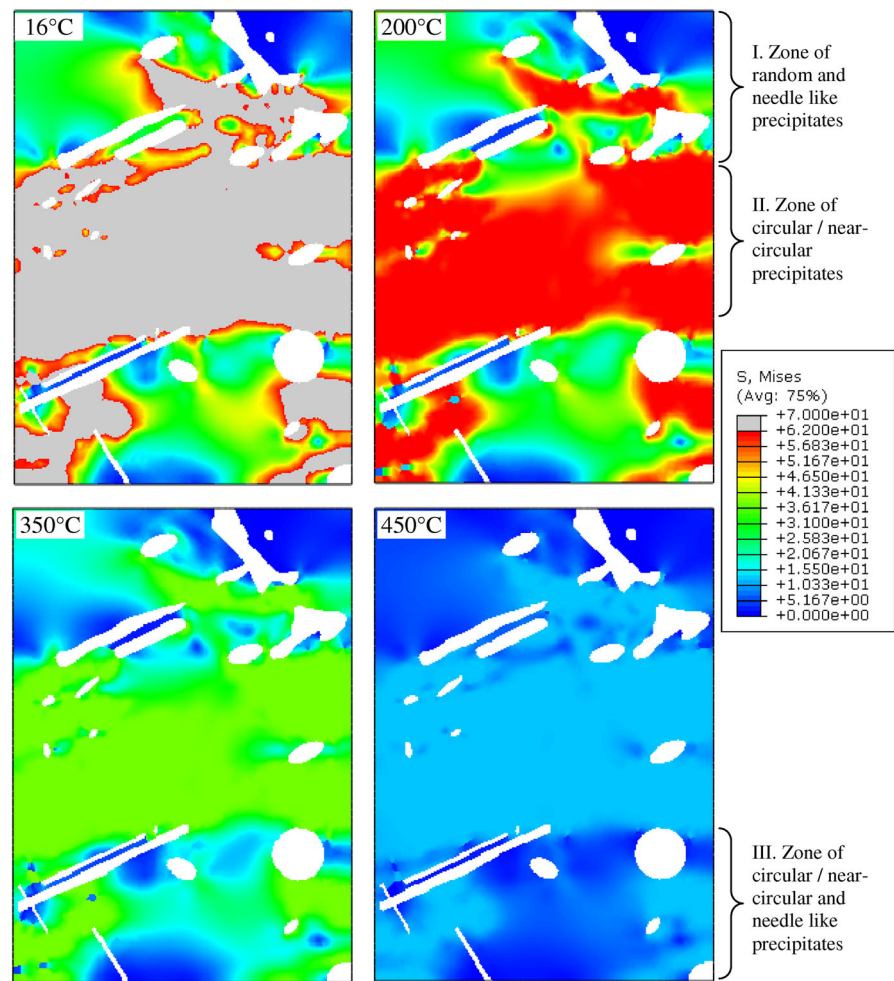
incoherent precipitates impart discontinuous characteristics to the parent matrix.

It may be observed that the change in temperature only affects the maximum stress acquired and not the distribution. For instance, note the difference between simulated microstructures at 16 and 450 °C. Apparently, the latter is almost unstressed compared to the former, which is, in fact, an effect of the temperature softening (i.e. improved dislocation glide, climb etc.). Nevertheless, the microstructures can be sub-divided into three distinct zones with respect to the precipitate shape morphology (see Fig. 9). Here, zones I and III comprise of random, circular and needle-like precipitates. The excess of precipitates leads to irregular deformation and hence alter the stress distribution. Zone II, however, contains only circular/near-circular impurities, which results in the uniform distribution of stress over a larger area. This further means that randomly distributed needle-like 'incoherent' precipitates severely influence the matrix stress field, while circular incoherent precipitates affect very small regions in their vicinity. It may, therefore, be stated that a desired state of stress can be achieved by controlling the precipitate volume fraction and shape.

4.4 Coherent and incoherent precipitates: stress fields

Having discussed the limiting cases of completely coherent and completely incoherent precipitates, it is of interest to analyze the situation where a combination of coherent and incoherent precipitates is present. Besides, the shape morphology of precipitates (see Fig. 2) also suggests that the needle-like precipitates are coherent, while near-circular ones are incoherent. Figure 10 compares the three cases of (a) only coherent (b) coherent + incoherent and (c) only incoherent precipitates at 16 °C. Note that the transformation of circular impurities from coherent (Fig. 10a) to incoherent (Fig. 10b) precipitates imparts not only a non-uniformity to the matrix stress field but also alters the stress state of the needle-like precipitates. The maximum stress in needle-like coherent precipitates reaches up to 1061 MPa in case of all coherent precipitates, while it remains 578 MPa in case of the combination of coherent and incoherent precipitates. It implies that the resistance to deformation offered by the latter (case b) is almost twice as less as the former (case a). It further indicates that the increasing fraction

Fig. 9 Von Mises stress (MPa) distribution in the α -matrix with incoherent precipitates at various temperatures



of incoherent precipitates results in a decreasing toughness of the material. In other words, the more the coherency loss, the weaker the material.

4.5 Coherent and incoherent precipitates: strain fields

The maximum principal plastic strain fields in the matrix due to completely coherent, completely incoherent and coherent + incoherent precipitates are shown in Figs. 11, 12 and 13, respectively. A comparison of the strain distribution at 100 and 450 °C is presented. Consider Fig. 11 at first; since the coherent precipitates have very high strength as compared to the α -matrix, they show minimum plastic deformation i.e. $<10^{-5}$, while the matrix deforms up to a strain value of 0.41. It is interesting to observe that

the strain distribution is identical at both the temperatures 100 and 450 °C with an only difference of peak strain values, which are 0.41 in the former and 0.32 in the latter case. Since the difference ($0.41 - 0.32 = 0.09$) is small over a large range of temperature, it can be inferred that the effect of change in temperature is less significant as long as the precipitates are coherent.

A considerable difference in the plastic strain state is, however, observed once the coherency is lost. This is quite obvious from Fig. 12, where not only the maximum plastic strain is 0.69, but also the strain distribution is significantly different. Note that the microstructure with coherent precipitates (Fig. 11) shows widespread plastic deformation in the entire matrix, whereas the one with incoherent precipitates (Fig. 12) depicts localized deformation in the vicinity

Fig. 10 Von Mises stress (MPa) distribution in the matrix with **a** only coherent **b** coherent + incoherent and **c** only incoherent precipitates at 16 °C

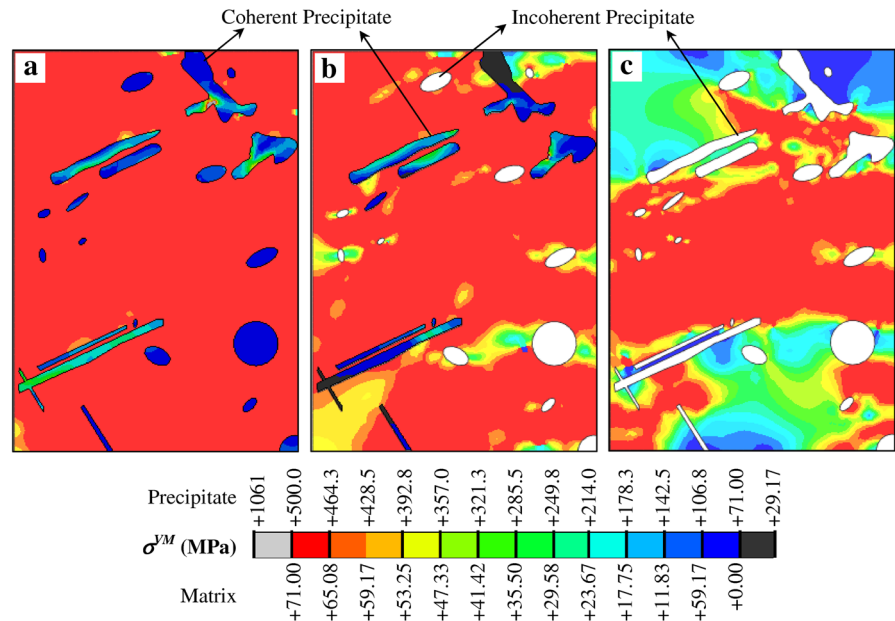
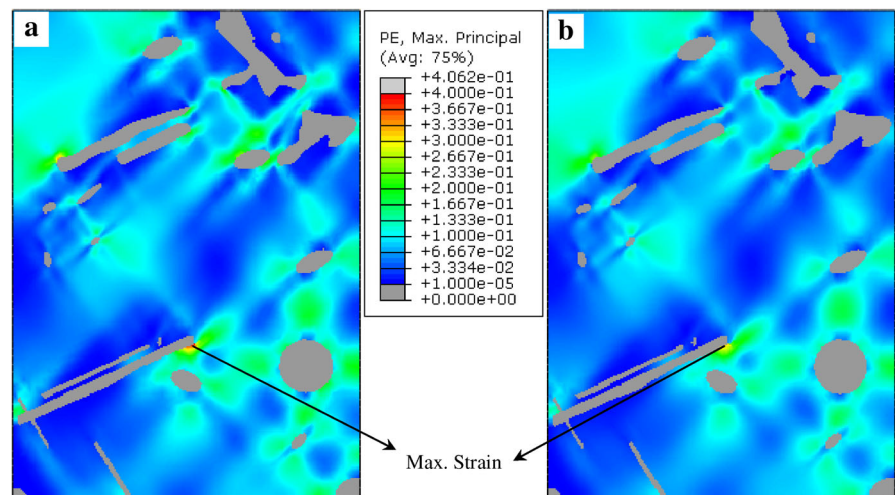


Fig. 11 Maximum principal strain in the matrix with coherent precipitates at **a** 100 °C and **b** 450 °C



of precipitates. It has been mentioned earlier that, unlike the incoherent impurities, the coherent precipitates offer continuity of the medium. It is, hence, the continuity effect that is reflected here too. Once again the plastic strain states in Fig. 12 at 100 and 450 °C resemble each other; yet a nontrivial difference is observed between the acquired peak strains, 0.39 for the former and 0.69 for the latter. Here, not only the difference ($0.69 - 0.39 = 0.3$) is considerably large in comparison to coherent precipitates, but also the locations for peak strain values are different.

Figure 13 features the effects of both the coherent and incoherent precipitates. Here, the peak strain values are 0.63 and 0.46 at 100 and 450 °C, respectively, and their difference is ($0.63 - 0.46 = 0.17$), i.e. midway between the completely coherent and completely incoherent precipitates. Clearly, the damage will initiate in the highly strained regions. Compared to Figs. 11 and 12, it is rather easier to predict the path along which failure of the material is more likely to occur.

Another important observation is that the localized plastic strain follows a well defined pattern (Figs. 12

Fig. 12 Maximum principal strain in the matrix with incoherent precipitates at **a** 100 °C and **b** 450 °C

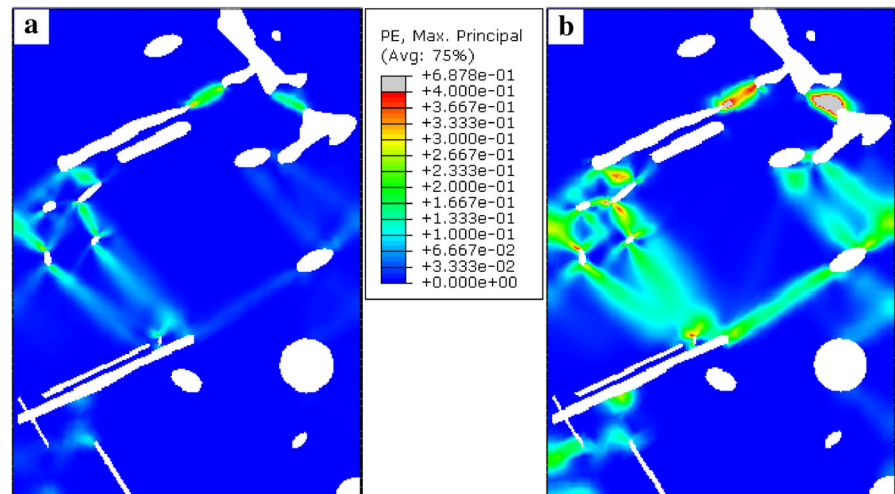
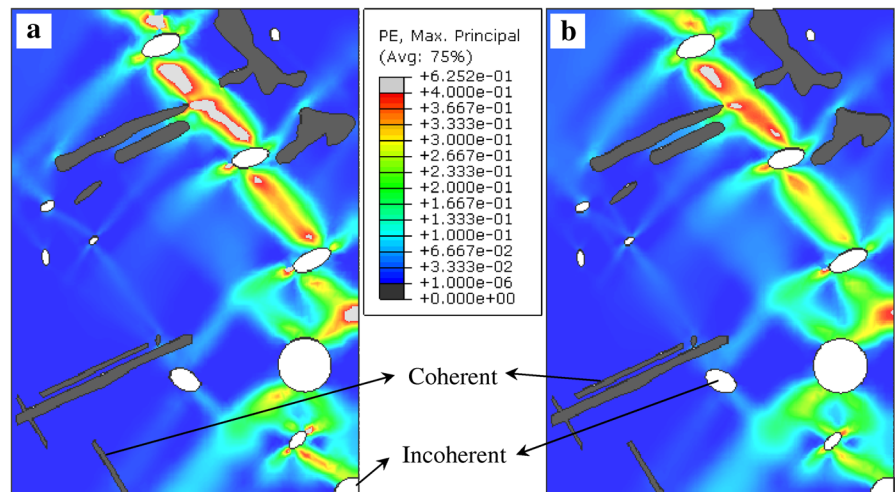


Fig. 13 Maximum principal strain in the matrix with coherent + incoherent precipitates at **a** 100 °C and **b** 450 °C



and 13). Circular/near-circular impurities show negligible deformation of the matrix when they are isolated. They, however, develop a sort of deformation ‘network’ when present near a needle-like or random precipitate. Highly strained regions are present at the end points of needles or between the random particles. If the needles are aligned in such a way that their end points are close to each other, they develop a continuously deformed region. An identical pattern may also be observed in Fig. 11; however, the plastic strains, instead of being concentrated, are more ‘diffused’ here. This is because the ability of the coherent precipitates to withstand high stresses does not allow uneven deformation of the soft α -matrix. It can, therefore, be stated that the regions of highly

concentrated localized strains due to incoherent precipitates are responsible for an increased likelihood of damage, whereas a distributed near-uniform plastic deformation due to coherent precipitates provides more allowance for the deformation before fracture.

4.6 Grain size effect

Given that the yield strength is a function of grain size (d), it is important to investigate the effect of grain size upon the stress state of the microstructure. As mentioned earlier, the grain size was assumed to vary from 10 to 200 μm . An average value of Hall–Petch parameter (K_{HP-avg}) was calculated using Fig. 5b. Figure 14 presents the yield strength values of the

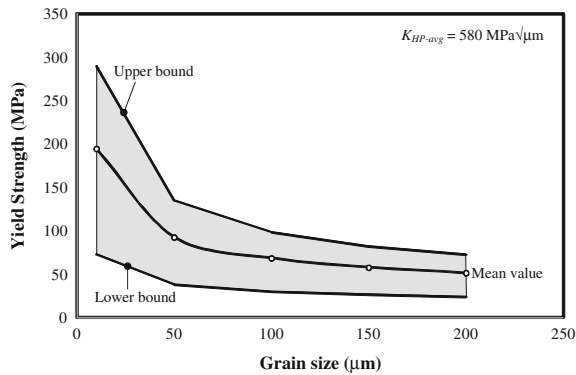


Fig. 14 Yield strength of matrix as a function of grain size

matrix in relation to the grain size, where upper and lower bounds are shown in addition to the mean values. It is to be noted that a smaller grain size leads to a wide range (upper limit–lower limit) of σ_y . Since σ_y of homogeneous material at room temperature remains around 233 MPa (see Fig. 7), any value greater than this value in Fig. 14 is obviously unacceptable. It has been explained previously that for fine grain size (around 10 μm or less) yield strength is sensitive to the distribution of grains. It is for this reason that the effect of grain size $<10 \mu\text{m}$ is not considered in the present work.

The FE simulations were performed using the mean values of yield strength with the grain size of 10, 50, 100, 150 and 200 μm . Figure 15 demonstrates the von Mises stress state within the α -matrix along with coherent + incoherent precipitates for the grain sizes of 10, 100, and 200 μm . Note that the grain size affects only the peak stress level and not the stress distribution. It has been shown in the previous sections that the stress distribution is dictated by the nature and morphology of precipitates (coherent, incoherent or a combination of both). It may be observed from Fig. 15 that the peak von Mises stresses in the matrix reach 194.3, 68.3 and 51.2 MPa for the corresponding grain size of 10, 100, and 200 μm , respectively. These values suggest that for a given type and behavior of precipitates the matrix with $d = 10 \mu\text{m}$ behaves almost three and four times as strong as the ones with $d = 100 \mu\text{m}$ and $d = 200 \mu\text{m}$, respectively. Likewise, for a prescribed level of strain, the precipitates surrounded by smaller grains ($d = 10 \mu\text{m}$) experience maximum stress level ($\sigma^{VM} = 1208 \text{ MPa}$) in comparison to the larger grains where the Mises stress is twice

as less, i.e. $\sigma^{VM} = 568 \text{ MPa}$ for $d = 100 \mu\text{m}$ and $\sigma^{VM} = 450 \text{ MPa}$ for $d = 200 \mu\text{m}$.

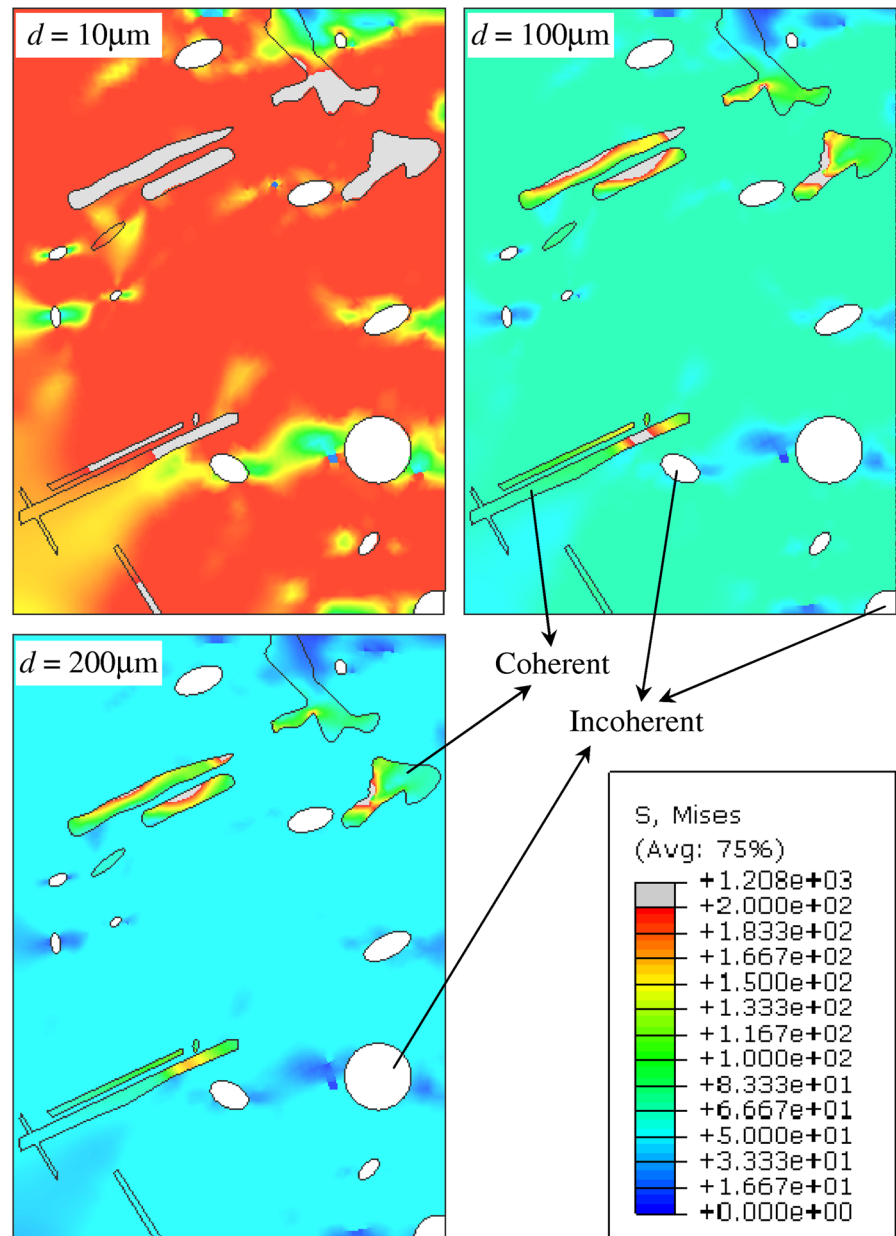
One of the limitations of the current model is that it assumes the presence of only one of the grain sizes (10, 50, 100, 150 or 200 μm) and not the combination of grains of different sizes. Although this assumption is safe because the area under consideration is small ($0.542 \mu\text{m} \times 0.387 \mu\text{m}$), the real situation is somewhat different since the HAZ is composed of a range of different sized grains, where the grain size is smallest immediately next to the weld bead and increases gradually away from it. Improvement in the current model with respect to the distribution of grains may be treated in some later work.

5 Conclusions

The numerical analysis of 6xxx series alloys at macro- and micro-scale has been carried out to explore the 2D stress and strain fields due to coherent and incoherent precipitates. Based on the findings and above discussion, several conclusions can be drawn:

- The macro-simulation ensured uniform distribution of temperature and stress over a considerable area within the gauge length. This was important because the micro-stress and strain fields were to be simulated at a single test temperature.
- The theoretical yield strength of hard precipitates (Mg_xSi_y) is several orders of magnitude higher than that of the homogeneous bulk material. In order to correctly model the microstructure, it is important to know the thermo-physical properties of each constituent as accurately as possible. Since the Mori–Tanaka model for the estimation of material properties takes into account the volume fraction as well as shape morphology of the impurities, it was deemed sufficient to estimate the unknown parameters.
- Although coherent precipitates of different shapes may be present in the microstructure, the randomly coalesced impurities are the most critical ones with respect to the peak stress values and hence are more likely to favor the crack initiation. The circular precipitates, however, would be the last to reach fracture or decohesion stress.
- While the resistance to deformation is influenced greatly by the loss of coherency in 6xxx series

Fig. 15 Grain size effect on Von Mises stress (MPa) in the matrix with coherent + incoherent precipitates



alloys; it is actually the highly non-uniform stress field induced throughout the matrix that divulges the reason for reduced strength and hardness. The more the incoherent precipitates per unit area, the more the stress field is non-uniform. The effect of isolated circular impurities, however, is trivial.

- Very high strength of the coherent precipitates results in their minimum plastic deformation.

Moreover, the plastic strain field in the soft matrix due to the coherent precipitates is more uniform and less in magnitude than the one due to the incoherent impurities, since the latter introduces discontinuities at the micro-scale.

- Grain size was found to influence the strength of 6xxx series alloy such that the smaller grain size yields improved resistance to deformation and vice versa.

The difference between the coherent and semi-coherent precipitates was not taken care of in the present work. The role of each type of precipitate can be further investigated in the future work.

Acknowledgments This work was funded by the Deanship of Scientific Research (DSR), King Abdulaziz University, Jeddah, under Grant No. 966-246-D1435. The authors, therefore, acknowledge with thanks DSR technical and financial support.

References

- Asserin-Lebert, A., Besson, J., Gourgues, A.F.: Fracture of 6056 aluminum sheet materials: effect of specimen thickness and hardening behavior on strain localization and toughness. *Mater. Sci. Eng., A* **395**, 186–194 (2005)
- ASM International: Wrought Aluminum (WA), Atlas of stress-strain curves, 2nd ed, pp. 414. ASM International, Materials Park, OH, USA (2002)
- Bardel, D., Perez, M., Nelias, D., Deschamps, A., Hutchinson, C.R., Maissonnette, D., Chaise, T., Garnier, J., Bourlier, F.: Coupled precipitation and yield strength modeling for non-isothermal treatments of a 6061 aluminium alloy. *Acta Mater.* **62**, 129–140 (2014)
- Berbenni, S., Favier, V., Berveiller, M.: Impact of the grain size distribution on the yield stress of heterogeneous materials. *Int. J. Plast.* **23**, 114–142 (2007)
- Cabibbo, M., McQueen, H.J., Evangelista, E., Spigarelli, S., Di Paola, M., Falchero, A.: Microstructure and mechanical property studies of AA 6056 friction stir welded plate. *Mater. Sci. Eng., A* **460–461**, 86–94 (2007)
- Cavaliere, P., Campanile, G., Panella, F., Squillace, A.: Effect of welding parameters on mechanical and microstructural properties of AA 6056 joints produced by Friction Stir Welding. *J. Mater. Process. Technol.* **180**, 263–270 (2006)
- Chakrabarti, D.J., Laughlin, D.E.: Phase relations and precipitation in Al–Mg–Si alloys with Cu additions. *Prog. Mater. Sci.* **49**, 389–410 (2004)
- Cicala, E., Duffet, G., Andrzejewski, H., Grevey, D., Ignat, S.: Hot cracking in Al–Mg–Si alloy laser welding—operating parameters and their effects. *Mater. Sci. Eng., A* **395**, 1–9 (2005)
- Darcourt, C., Roelandt, J.M., Rachik, M., Deloison, D., Journet, B.: Thermomechanical analysis applied to the laser beam welding simulation of aeronautical structures. *J. Phys. IV* **120**, 785–792 (2004)
- Deschamps, A., Brechet, Y.: Influence of predeformation and ageing of Al–Zn–Mg alloy—II. Modeling of precipitation kinetics and yield stress. *Acta Mater.* **47**, 293–305 (1999)
- Edwards, G.A., Stiller, K., Dunlop, G.L., Couper, M.J.: The precipitation sequence in Al–Mg–Si alloys. *Acta Mater.* **46**, 3893–3904 (1998)
- Gallais, C., Denquin, A., Bréchet, Y., Lapasset, G.: Precipitation microstructures in an AA6056 aluminium alloy after friction stir welding: characterisation and modelling. *Mater. Sci. Eng., A* **496**, 77–89 (2008)
- Hall, E.O.: The deformation and ageing of mild Steel III—discussion of results. *Proc. Phys. Soc. Lond. Sect. B* **64**(381), 747–753 (1951)
- Hashin, Z., Shtrikman, S.: A variational approach to the theory of the effective magnetic permeability of multiphase materials. *J. Appl. Phys.* **33**, 3125–3131 (1962)
- Heinz, A., Haszler, A., Keidel, C., Moldenhauer, S., Benedictus, R., Miller, W.S.: Recent development in aluminium alloys for aerospace applications. *Mater. Sci. Eng., A* **280**, 102–107 (2000)
- Josserand, E., Jullien, J.F., Nelias, D., Deloison, D.: Numerical simulation of welding-induced distortions taking into account industrial clamping conditions. *Math. Model. Weld. Phenom.* **8**, 1105–1124 (2007)
- Kocks, U.F., Argon, A.S., Ashby, M.F.: Thermodynamics and kinetics of slip. *Prog. Mater. Sci.* **19**, 1 (1975)
- Ledbetter, H.M.: Temperature behaviour of Young moduli of 40 engineering alloys. *Cryogenics* **22**(12), 653–656 (1982)
- Liu, J., Kulak, M.: A new paradigm in the design of aluminium alloys for aerospace applications. *Mater. Sci. Forum* **331–337**, 127–140 (2000)
- Maissonnette, D., Suery, M., Nelias, D., Chaudet, P., Epicier, T.: Effects of heat treatments on the microstructure and mechanical properties of a 6061 aluminium alloy. *Mater. Sci. Eng., A* **528**(6), 2718–2724 (2011)
- Matsuda, K., Ikeno, S., Sato, T.: HRTEM study of nano-precipitation phases in 6000 series aluminum alloys. *Sci. Technol. Educ. Microsc. Overv.* **1**, 152–162 (2003)
- Miao, W.F., Laughlin, D.E.: Precipitation hardening in aluminum alloy 6022. *Scr. Mat.* **40**, 873–878 (1999)
- Mori, T., Tanaka, K.: Average stress in matrix and average elastic energy of materials with misfitting inclusions. *Acta Met.* **21**, 571–574 (1973)
- Nélias, D., Zain-ul-Abdein, M., Maissonnette, D.: Thermomechanical industrial processes. In: Bergheau, J.M. (ed.) *Laser and electron beam welding of 6xxx series aluminum alloys: on some thermal, mechanical and metallurgical aspects*, pp. 75–153. Wiley, Hoboken (2014). doi:[10.1002/9781118578759.ch2.75-153](https://doi.org/10.1002/9781118578759.ch2.75-153)
- Petch, N.J.: The cleavage strength of polycrystals. *J. Iron Steel Inst.* **174**(1), 25–28 (1953)
- Porter, D.A., Easterling, K.E.: *Phase transformations in metals and alloys*, 2nd edn, pp. 291–303. Chapman and Hall, London (1992)
- Radaj, D.: *Heat effects of welding*. Pergamon Press, New York (1992)
- Riahi, M., Nazari, H.: Analysis of transient temperature and residual thermal stresses in friction stir welding of aluminum alloy 6061-T6 via numerical simulation. *Int. J. Adv. Manuf. Technol.* **55**(1–4), 143–152 (2011)
- Schwartzberg, F.R., Osgood, S.H., Herzog, R.G., Knight, M.: *Cryogenic materials data handbook (revised)*. AFML-TDR-64-280, AD713619 **1**, (1970)
- Sharma, S.C.: Effect of albite particles on the coefficient of thermal expansion behavior of the Al6061 alloy composites. *Metall. Mater. Trans. A* **31A**, 773–780 (2000)
- Silcock, J.M., Heal, T.J., Hardy, H.K.: Structural ageing characteristics of binary aluminium–copper alloys. *J. Inst. Metals.* **82**, 239 (1954)
- Simar, A., Brechet, Y., de Meester, B., Denquin, A., Gallais, C., Pardoën, T.: Integrated modeling of 6xxx series Al alloys: process, microstructure and properties. *Prog. Mater. Sci.* **57**, 95–183 (2012)

- Wiener, O.: Die Theorie des Mischkörpers für das Feld der stationären Stromung. Erste Abhandlung die Mittelwertsätze für Kraft, Polarisierung und Energie. Abhandlungen der Mathematisch-Physischen Klasse der Königlich-Sächsischen Gesellschaft der Wissenschaften **32**(6), 509–604 (1912)
- Zain-ul-abdein, M., Nélias, D., Jullien, J.F., Wagan, A.I.: Thermo-mechanical characterisation of AA 6056-T4 and estimation of its material properties using genetic algorithm. Mater. Des. **31**, 4302–4311 (2010a)
- Zain-ul-abdein, M., Nélias, D., Jullien, J.F., Deloison, D.: Experimental investigation and finite element simulation of laser beam welding induced residual stresses and distortions in thin sheets of AA 6056-T4. Mater. Sci. Eng., A **527**, 3025–3039 (2010b)
- Zhang, J., Shen, Y., Li, B., Xu, H., Yao, X., Kuang, B., Gao, J.: Numerical simulation and experimental investigation on friction stir welding of 6061-T6 aluminum alloy. Mater. Des. **60**, 94–101 (2014)